Available online at www.sciencedirect.com
ScienceDirect
Journal of Computational Physics 227 (2008) 3015–3031
JOURNAL OF COMPUTATIONAL PHYSICS
www.elsevier.com/locate/jcp

Efficient kinetic schemes for steady and unsteady flow simulations on unstructured meshes

Guoxi Ni [a,*], Song Jiang [a], Kun Xu [b]

[a] LCP, Institute of Applied Physics and Computational Mathematics, P.O. Box 8009, Beijing 100088, China
[b] Department of Mathematics, Hong Kong University of Science and Technology, Clear Water Bay, Kowloon, Hong Kong

Received 28 August 2006; received in revised form 10 May 2007; accepted 8 June 2007
Available online 29 June 2007

Abstract

This paper presents efficient second-order kinetic schemes on unstructured meshes for both compressible unsteady and incompressible steady flows. For compressible unsteady flows, a time-dependent gas distribution function with a discontinuous particle velocity space at a cell interface is constructed and used for the evaluations of both numerical fluxes and conservative flow variables. As a result, a compact scheme on the unstructured meshes is developed. For incompressible steady flows, a continuous second-order gas-kinetic BGK type scheme is presented, for which the time-dependent gas distribution function with a continuous particle velocity is used on unstructured meshes. The efficiency of the schemes lies in the fact that the slopes of the flow variables inside each cell can be constructed using values of the flow variables within that cell only without involving neighboring cells. Therefore, even with the stencil of a first-order scheme, a high resolution method is constructed. Numerical examples are presented which are compared with the benchmark solutions and the experimental measurements.
© 2008 Elsevier Inc. All rights reserved.

Keywords: Compressible unsteady flows; Incompressible steady flows; Efficient second-order kinetic schemes; Unstructured meshes

1. Introduction

Great progress has been achieved in the area of computational fluid dynamics (CFD) in the past decades. The developments of advanced numerical algorithms have made the CFD a valuable and indispensable tool in the analysis of highly complex flow problems. However, the construction of highly accurate and reliable numerical methods is still under demand as the geometry and flow physics become more sophisticated.

In recent years, the development of Boltzmann-type schemes has attracted much attention. The success of such schemes has appeared in a wide range of engineering applications, see for example, [13,14,8,15]. Among the Boltzmann-type schemes, the equilibrium-flux method (EFM) has been intensively studied [17]. EFM is a flux splitting method and is also referred to as a kinetic flux vector splitting (KFVS) scheme [17]. In fact, the EFM and KFVS schemes are identical. The KFVS scheme is composed of two steps. Firstly, the free transport equation or the col-

* Corresponding author. Tel.: +86 10 62057509x2968; fax: +86 10 62057289.
E-mail addresses: gxni@iapcm.ac.cn (G. Ni), jiang@iapcm.ac.cn (S. Jiang), makxu@ust.hk (K. Xu).

0021-9991/$ - see front matter © 2008 Elsevier Inc. All rights reserved.
doi:10.1016/j.jcp.2007.06.018

lisionless Boltzmann equation is solved in the gas evolution stage for the flux evaluation. Then, the collision part is implicitly implemented through the preparation of a new equilibrium state inside each cell at the beginning of next time step. With the inclusion of Boltzmann collision model in the flux evaluation process, the gas-kinetic BGK scheme has been proposed in [2,6,20]. The BGK scheme differs from the KFVS method mainly in the inclusion of particle collisions in the gas evolution stage. Instead of solving the collisionless Boltzmann equation, the particle transport in the BGK scheme is controlled by a real particle collision time, which is related to the physical dissipative coefficients. In other words, instead of using the numerical time step as the particle collision time in the KFVS scheme, the real physical collision is included in the BGK scheme, where the accurate Navier–Stokes solutions have been obtained (cf. [21,22]). Since the gas evolution process is associated with a relaxation process, i.e. from a non-equilibrium state to an equilibrium one, the entropy condition is always satisfied by the BGK scheme. In the smooth region, where the physical structure can be well resolved by the numerical cell size, the BGK scheme gives an accurate compressible Navier–Stokes solution. In the discontinuity region, a delicate dissipative mechanism in the BGK scheme generates a stable and crisp shock transition.

The gas-kinetic BGK scheme is a finite volume method which originally targets on the simulation of compressible flows. In order to further extend its applicability, in this paper we construct a new efficient second-order kinetic schemes for compressible unsteady and incompressible steady flows on unstructured meshes. Here, a second-order method means that the reconstructed equilibrium and non-equilibrium states have piecewise linear distributions in space. At the same time, as analyzed in [16], in the smooth region the time accuracy of the scheme is equivalent to the Lax–Wendroff method for the Navier–Stokes equations. For the sake of clear presentation, in this paper we will restrict the presentation of our schemes only in two-dimensional space. However, the schemes of this paper can be straightforwardly extended to the three-dimensional case without any essential difficulty.

The basic idea in the construction of our efficient kinetic schemes lies in the fact that from a time accurate gas distribution function at a cell interface, we can not only calculate the numerical fluxes, but also evaluate accurate flow variables. Therefore, based on the cell averaged conservative flow variables and their cell interface values, we can construct or update the slopes within a cell solely. In other words, even with a stencil of a first-order scheme, a high resolution scheme can be still constructed. In this way, we avoid using the flow variables from neighboring cells in the construction of limited slopes. This is different from a traditional finite volume method, especially for a high-order scheme (see [11,14] for example). So, using a compact stencil we are able to construct an efficient gas-kinetic BGK scheme, which is computationally cheap and easy in coding. As is well-known, sometimes it is very difficult to choose a suitable stencil to construct all slopes on unstructured meshes. For incompressible steady flow simulation, the numerical dissipation introduced in the gas-kinetic BGK scheme through discontinuities of flow variables at a cell interface needs to be eliminated. In this case, a continuous gas distribution function corresponding to an isothermal flow is constructed for both flux evaluation and flow variables update at a cell interface. This is similar to the Lattice Boltzmann approach, where the solution in the isothermal low Mach number limit is obtained.

This paper is organized as follows. In Section 2, the gas-kinetic BGK model for compressible and incompressible isothermal flows is presented. Section 3 is devoted to the construction of the efficient second-order kinetic schemes on unstructured meshes. Section 4 present numerical examples which demonstrate the efficiency and accuracy of the schemes in the simulation of compressible and incompressible flows. The last section is the conclusion.

2. BGK model for compressible and incompressible isothermal flows

The BGK model in two space dimensions can be written as

$$f_t + uf_x + vf_y = \frac{g - f}{\tau}, \tag{2.1}$$

where f is the gas distribution function and g is the equilibrium state approached by f, (u, v) is the particle velocity. Both f and g are functions of x, y, t, u, v and the internal variable ξ. The particle collision time τ is related to the viscosity coefficient.

Generally, the equilibrium state is a Maxwellian distribution

$$g = \rho\left(\frac{\lambda}{\pi}\right)^{\frac{K+2}{2}} e^{-\lambda((u-u)^2+(v-v)^2+\xi^2)}, \tag{2.2}$$

where ρ is the macroscopic density, λ is equal to $m/(2kT)$, m is the molecular mass, k is the Boltzmann constant, and T is the temperature. The total number of degree of freedom K in ξ is equal to $(4-2\gamma)/(\gamma-1)$, and ξ^2 denotes $\xi^2 = \xi_1^2 + \xi_2^2 + \cdots + \xi_K^2$.

The relation between the mass ρ, the momentum $(\rho U, \rho V,)$, the energy E and the distribution function f is given by

$$(\rho, \rho U, \rho V, E)^{\mathrm{T}} = \int \Psi f \, \mathrm{d}\Xi,$$

where

$$\Psi = (\psi_1, \psi_2, \psi_3, \psi_4)^{\mathrm{T}} = \left(1, u, v, \frac{1}{2}(u^2 + v^2 + \xi^2)\right)^{\mathrm{T}},$$

and $\mathrm{d}\Xi = \mathrm{d}u\,\mathrm{d}v\,\mathrm{d}\xi$ is the volume element in the phase space.

Since the mass, momentum, and energy are conservative during particle collisions, f and g satisfy the conservation constraints

$$\int (g - f)\psi_\alpha \, \mathrm{d}\Xi = 0, \quad \alpha = 1, 2, 3, 4,$$

at any point in space and time.

For a local equilibrium state with $f = g$, the Euler equations can be obtained by taking the moments of Ψ to Eq. (2.1), and the corresponding Euler equations are

$$\begin{pmatrix} \rho \\ \rho U \\ \rho V \\ E \end{pmatrix}_t + \begin{pmatrix} \rho U \\ \rho U^2 + p \\ \rho UV \\ (E+p)U \end{pmatrix}_x + \begin{pmatrix} \rho V \\ \rho UV \\ \rho V^2 + p \\ (E+p)V \end{pmatrix}_y = 0,$$

where $E = \frac{1}{2}\rho(U^2 + V^2 + (K+2)/(2\lambda))$ is the total energy and $p = \rho/(2\lambda)$ is the pressure.

On the other hand, to the first order of τ, the Chapman–Enskog expansion gives $f = g - \tau(g_t + ug_x + vg_y)$ [21]. Taking moments Ψ to the BGK Eq. (2.1) with this f, we get

$$\int (g_t + ug_x + vg_y)\Psi \, \mathrm{d}\Xi = \tau \int (g_{tt} + 2ug_{xt} + u^2 g_{xx} + 2vg_{yt} + 2uvg_{xy} + v^2 g_{yy})\Psi \, \mathrm{d}\Xi,$$

from which the compressible Navier–Stokes equations with dynamic viscous coefficient $\mu = \tau p$ can be obtained

$$\begin{pmatrix} \rho \\ \rho U \\ \rho V \\ E \end{pmatrix}_t + \begin{pmatrix} \rho U \\ \rho U^2 + p \\ \rho UV \\ (E+p)U \end{pmatrix}_x + \begin{pmatrix} \rho V \\ \rho V \\ \rho V^2 + p \\ (E+p)V \end{pmatrix}_y = \begin{pmatrix} 0 \\ s_{1x} \\ s_{2x} \\ s_{3x} \end{pmatrix}_x + \begin{pmatrix} 0 \\ s_{1y} \\ s_{2y} \\ s_{3y} \end{pmatrix}_y, \tag{2.3}$$

where

$$\begin{aligned}
s_{1x} &= \tau p\left[2\tfrac{\partial U}{\partial x} - \tfrac{2}{K+2}\tfrac{\partial U}{\partial x} + \tfrac{\partial V}{\partial y}\right], \\
s_{2x} &= \tau p\left[\tfrac{\partial V}{\partial x} + \tfrac{\partial V}{\partial y}\right], \\
s_{3x} &= \tau p\left[2U\tfrac{\partial U}{\partial x} + V\left(\tfrac{\partial V}{\partial x} + \tfrac{\partial U}{\partial y}\right) - \tfrac{2U}{K+2}\left(\tfrac{\partial U}{\partial x} + \tfrac{\partial V}{\partial y}\right) + \tfrac{K+4}{4}\tfrac{\partial}{\partial x}\left(\tfrac{1}{\lambda}\right)\right], \\
s_{1y} &= \tau p\left[2\tfrac{\partial U}{\partial y} + \tfrac{\partial V}{\partial x}\right], \\
s_{2y} &= \tau p\left[\tfrac{\partial V}{\partial y}\tfrac{2}{K+2}\left(\tfrac{\partial U}{\partial x} + \tfrac{\partial V}{\partial y}\right)\right], \\
s_{3y} &= \tau p\left[U\tfrac{\partial U}{\partial y} + V\left(\tfrac{\partial V}{\partial x} + 2V\tfrac{\partial V}{\partial y}\right) - \tfrac{2}{K+2}U\left(\tfrac{\partial U}{\partial x} + \tfrac{\partial V}{\partial y}\right) + \tfrac{K+4}{4}\tfrac{\partial}{\partial y}\left(\tfrac{1}{\lambda}\right)\right].
\end{aligned}$$

In order to accurately approximate the incompressible flow limit, the isothermal model is usually used in many pseudo-compressible codes, such as in the Lattice Boltzmann method (see, e.g. [4]). For an isothermal flow, λ in the equilibrium state (2.2) becomes a constant. In order to closely approach the incompressible limit, which is equivalent to the increasing of the fluid sound speed, the largest value of γ has to be used, which is $\gamma = 2$. Therefore, for the isothermal incompressible flow, the equilibrium state in the BGK model can be approximated as

$$g = \rho\left(\frac{\lambda}{\pi}\right)\mathrm{e}^{-\lambda((u-U)^2+(v-V)^2)}, \tag{2.4}$$

where

$$\lambda = \frac{1}{2\theta}, \quad \text{and} \quad \theta = \frac{kT}{m},$$

and both T and θ are constants.

The relation between the mass ρ, the momentum $(\rho U, \rho V)$ and the distribution function in the isothermal flow case is given by

$$(\rho, \rho U, \rho V)^{\mathrm{T}} = \int \Phi f \,\mathrm{d}\Xi,$$

where

$$\Phi = (\psi_1, \psi_2, \psi_3)^{\mathrm{T}} = (1, u, v)^{\mathrm{T}},$$

and $\mathrm{d}\Xi = \mathrm{d}u\,\mathrm{d}v$ is the volume element in the phase space.

Since the mass and momentum are conservative during the particle collisions, f and g should satisfy the conservation constraints

$$\int (g - f)\psi_\alpha \,\mathrm{d}\Xi = 0, \quad \alpha = 1, 2, 3,$$

at any point in space and time.

Based on the Chapman–Enskog expansion, a distribution function

$$f = g - \tau(g_t + ug_x + vg_y) \equiv g + f^{(1)}$$

is used to derive the isothermal Navier–Stokes equations. Taking moments Φ to Eq. (2.1) with the above f leads to

$$\int \psi_\alpha (f_t + uf_x + vf_y)\,\mathrm{d}\Xi = 0, \quad \alpha = 1, 2, 3,$$

and the corresponding equations are

$$\frac{\partial}{\partial t}\begin{pmatrix}\rho\\ \rho\mathbf{u}\end{pmatrix} + \mathrm{div}\begin{pmatrix}\rho\mathbf{u}\\ \rho\mathbf{u}\otimes\mathbf{u} + \rho\theta\mathbf{I}\end{pmatrix} = \begin{pmatrix}0\\ -\mathrm{div}\Pi\end{pmatrix}, \tag{2.5}$$

where $\mathbf{I}$ is the unit matrix, and

$$\mathbf{u} = (U, V), \quad \Pi = \{\Pi_{ij}\}, \quad p = \frac{\rho}{2\lambda},$$

$$\Pi_{ij} = \int f^{(1)}\xi_i\xi_j \,\mathrm{d}u\,\mathrm{d}v = -\tau\rho\theta(\partial_i U_j + \partial_j U_i - \partial_k U_k), \quad (\xi_1, \xi_2) \equiv (u, v).$$

In the incompressible limit, i.e. $\rho \sim$ constant, the kinematic viscosity in Π becomes $\nu = \tau\theta$.

3. Efficient second-order kinetic schemes on unstructured meshes

In this section, we present new second-order finite volume gas-kinetic schemes on unstructured meshes for compressible and incompressible isothermal flows. The general solution f of (2.1) at any point $\vec{x} = (x, y)$ and time t is given by

$$f(x,y,t,u,v) = \frac{1}{\tau}\int_0^t g(x',y',t',u,v)\mathrm{e}^{-(t-t')/\tau}\,\mathrm{d}t' + \mathrm{e}^{-t/\tau}f_0(x-ut,y-vt), \tag{3.1}$$

where $x' = x - u(t-t')$ and $y' = y - v(t-t')$.

Let Ω_j denote a mesh cell with edges e_k. The cell averaged conservative variables at the nth time level on the cell Ω_j are denoted for a compressible flow by

$$w_j^n = (\rho_j^n, \rho_j^n U_j^n, \rho_j^n V_j^n, E_j^n)$$

and for an incompressible isothermal flow by

$$w_j^n = (\rho_j^n, \rho_j^n U_j^n, \rho_j^n V_j^n),$$

respectively. We also denote by

$$\mathrm{d}w_{j,j+1/2}^n, \quad \mathrm{d}w_{j,j-1/2}^n, \quad \text{and} \quad \mathrm{d}w_{j,j-3/2}^n$$

the directional derivative at the nth time level along the normal direction of a cell interface between the cells j and $j+1$, the cells j and $j-1$, and the cells j and $j-2$, respectively (see Fig. 1).

Taking moments to the BGK Eq. (2.1) on the cell Ω_j, we get

$$\int_{\Omega_j}\int \psi_\alpha(f_t + uf_x + vf_y)\mathrm{d}\Xi\,\mathrm{d}X = 0,$$

where $\mathrm{d}X = \mathrm{d}x\,\mathrm{d}y$, or equivalently,

$$\frac{\mathrm{d}}{\mathrm{d}t}\int_{\Omega_j}\int \psi_\alpha f\,\mathrm{d}\Xi\,\mathrm{d}X + \int_{\Omega_j}\int (uf_x + vf_y)\mathrm{d}\Xi\,\mathrm{d}X = 0.$$

The above equation can be written as

$$\frac{\mathrm{d}}{\mathrm{d}t}\int_{\Omega_j}\int \psi_\alpha f\,\mathrm{d}\Xi\,\mathrm{d}X + \sum_{e_k\in\partial\Omega_j}\int \psi_\alpha f\vec{u}\cdot n\,\mathrm{d}\Xi\,\mathrm{d}S = 0, \tag{3.2}$$

where $\vec{u} = (u,v)^{\mathrm{T}}$, n denotes the external unit normal vector of the corresponding edge and e_k is the edge of the cell Ω_j. We write (3.2) in the form of a conservative scheme,

$$\frac{\mathrm{d}}{\mathrm{d}t}\int_{\Omega_j}\int \psi_\alpha f\,\mathrm{d}\Xi\,\mathrm{d}X + \sum_{e_k\in\partial\Omega_j}\mathcal{F}_{\psi_\alpha,e_k}(t)|e_k| = 0, \tag{3.3}$$

where $|e_k|$ is the measure of e_k and $\mathcal{F}_{\psi_\alpha,e_k}$ is the numerical flux across the cell edge e_k. The update of the corresponding macroscopic flow variables inside each control volume reads

$$w_j^{n+1} = w_j^n - \int_{t_n}^{t_{n+1}}\sum_{e_k\in\partial\Omega_j}\mathcal{F}_{w,e_k}(t)|e_k|/|\Omega_j|, \tag{3.4}$$

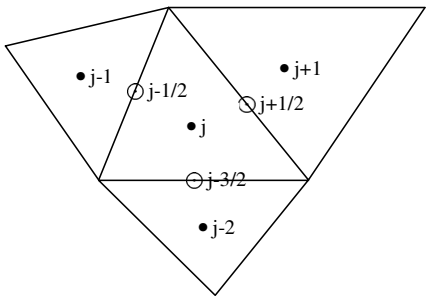

Fig. 1. Slope update scheme for discontinuous kinetic scheme, where dots are centroid of triangular cells, and circles are interface points.

where $|\Omega_j|$ is the measure of Ω_j. At the same time, the flow variables at the center of the edge can be evaluated as

$$w_{j,l}^{n+1} = \int \psi_\alpha f(x_{j,l}, t, u, v, \xi)\, \mathrm{d}\Xi,$$

where $l = j + 1/2, j - 1/2$, and $j - 3/2$. Thus, our numerical algorithm can be summarized as follows:

Given $(w_j^n, \mathrm{d}w_{j,j+1/2}^n, \mathrm{d}w_{j,j-1/2}^n, \mathrm{d}w_{j,j-3/2}^n)$ where $(\mathrm{d}w_{j,j+1/2}^n, \mathrm{d}w_{j,j-1/2}^n, \mathrm{d}w_{j,j-3/2}^n) = 0$ when $n = 0$, find $(w_j^{n+1}, \mathrm{d}w_{j,j+1/2}^{n+1}, \mathrm{d}w_{j,j-1/2}^{n+1}, \mathrm{d}w_{j,j-3/2}^{n+1})$ at the $(n+1)$th time level, where $\mathrm{d}w^{n+1}$ is constructed from the cell averaged and cell interface w.

From (3.4) we see that to obtain w_j^{n+1}, it suffices to construct the numerical flux $\mathcal{F}_{w,e_k}$. In the next section, based on the BGK model and with the help of the given $(w_j^n, \mathrm{d}w_{j,j+1/2}^n, \mathrm{d}w_{j,j-1/2}^n, \mathrm{d}w_{j,j-3/2}^n)$, we will show the way to construct $\mathcal{F}_{w,e_k}$.

3.1. An efficient second-order BGK solver for compressible flows

The numerical flux $\mathcal{F}_{w,e_k}$ is obtained based on the construction of an efficient second-order BGK solver along the normal direction of the edge e_k. We begin with rewriting (3.4) in componentwise:

$$\begin{cases} \rho_j^{n+1} = \rho_j^n - \int_{t_n}^{t_{n+1}} \sum\limits_{e_k \in \partial\Omega_j} \mathcal{F}_{\rho,e_k}(t)|e_k|/|\Omega_j|, \\ (\rho U)_j^{n+1} = (\rho U)_j^n - \int_{t_n}^{t_{n+1}} \sum\limits_{e_k \in \partial\Omega_j} \mathcal{F}_{\rho U,e_k}(t)|e_k|/|\Omega_j|, \\ (\rho V)_j^{n+1} = (\rho V)_j^n - \int_{t_n}^{t_{n+1}} \sum\limits_{e_k \in \partial\Omega_j} \mathcal{F}_{\rho V,e_k}(t)|e_k|/|\Omega_j|, \\ E^{n+1} = E^n - \int_{t_n}^{t_{n+1}} \sum\limits_{e_k \in \partial\Omega_j} \mathcal{F}_{E,e_k}(t)|e_k|/|\Omega_j|. \end{cases} \tag{3.5}$$

The first stage is to reconstruct the initial data, which is subsequently needed in the following dynamical evolution stage (the second stage) for the computation of gas distribution function at a cell interface.

By rotating the coordinates, we may assume the interface between the cell j and the cell $j+1$ to be $\Gamma_{j+1/2} := \{(x_{j+1/2}, y); -a < y < a\}$ for some $a > 0$, see Fig. 1, and without loss of generality we may take $x_{j+1/2} = 0$. For the compressible flow, the initial gas distribution f_0 at time $t = 0$ has the form

$$f_0 = \begin{cases} g^l[1 + a^l x - \tau(a^l u + A^l)], & x \leqslant 0, \\ g^r[1 + a^r x - \tau(a^r u + A^r)], & x \geqslant 0. \end{cases}$$

The equilibrium state g around $(x = 0, y = 0, t = 0)$ is assumed to be

$$g = g_0[1 + (1 - H(x))\overline{a}^l x + H(x)\overline{a}^r x] + \overline{A}t,$$

where $H(x)$ is the Heaviside function, and g and g_0 have the expression as that in (2.2). The coefficients $a^{l,r}, \overline{a}^{l,r}, A^{l,r}, \overline{A}$ are related to the derivatives of the Maxwellian in space and time, and assumed to have the following form obtained from a Taylor expansion of the Maxiwellian:

$$\begin{aligned} a^{l,r} &= a_1^{l,r} + a_2^{l,r}u + a_3^{l,r}v + \frac{1}{2}a_4^{l,r}(u^2 + v^2 + \xi^2), \\ \overline{a}^{l,r} &= \overline{a}_1^{l,r} + \overline{a}_2^{l,r}u + \overline{a}_3^{l,r}v + \frac{1}{2}\overline{a}_4^{l,r}(u^2 + v^2 + \xi^2), \\ A^{l,r} &= A_1^{l,r} + A_2^{l,r}u + A_3^{l,r}v + \frac{1}{2}A_4^{l,r}(u^2 + v^2 + \xi^2), \\ \overline{A} &= \overline{A}_1 + \overline{A}_2 u + \overline{A}_3 v + \frac{1}{2}\overline{A}_4(u^2 + v^2 + \xi^2), \end{aligned}$$

where $a_j^{l,r}, \overline{a}_j^{l,r}, A^{l,r}$ and $\overline{A}_j$ can be determined using the relation between the macroscopic variables and the gas distribution function [20]. For example, the coefficients a_j^l can be obtained by the following identity:

$$\int \begin{pmatrix} 1 \\ u \\ v \\ \frac{1}{2}(u^2+v^2+\xi^2) \end{pmatrix} \Big(a_1 + a_2 u + a_3 v + \frac{a_4}{2}(u^2+v^2+\xi^2)\Big) g \,\mathrm{d}\Xi = \begin{pmatrix} \frac{\partial \rho}{\partial n} \\ \frac{\partial \rho u}{\partial n} \\ \frac{\partial \rho v}{\partial n} \\ \frac{\partial E}{\partial n} \end{pmatrix} (\equiv \mathrm{d}w^n_{j,j+1/2}), \tag{3.6}$$

where $\frac{\partial}{\partial n}$ is the directional derivative along the normal direction of the cell interface between the cell j and the cell $j+1$. The coefficients A^l_j can be determined by the compatibility condition

$$\int (a^l u + A^l) \Psi g^l \,\mathrm{d}\Xi = 0$$

and the coefficients $\overline{A}$ by the conservative constrain condition over a time step

$$\int_0^{\Delta t} \int (g - f) \Psi \,\mathrm{d}t \,\mathrm{d}\Xi = 0.$$

Inserting g and f_0 into the solution (3.1) and recalling the definition of $H(x)$, we obtain the gas distribution function f at the cell interface $\Gamma_{j+1/2}$,

$$\begin{aligned} f(x_{j+1/2}, t, u, v, \xi) = {} & (1 - \mathrm{e}^{-t/\tau}) g_0 + [\tau(-1 + \mathrm{e}^{-t/\tau}) + t\mathrm{e}^{-t/\tau}][\overline{a}^l H(u) + \overline{a}^r (1 - H(u))] u g_0 \\ & + \tau\Big(\frac{t}{\tau} - 1 + \mathrm{e}^{-t/\tau}\Big)\overline{A} g_0 + \mathrm{e}^{-t/\tau}(1 - uta^l) H(u) g^l + \mathrm{e}^{-t/\tau}(1 - uta^r)(1 - H(u)) g^r \\ & + \mathrm{e}^{-t/\tau}(-\tau A^l H(u) g^l - \tau A^r (1 - H(u)) g^r), \end{aligned}$$

from which the flux across the cell interface $\Gamma_{j+1/2}$ is given by

$$\begin{pmatrix} \mathcal{F}_{\rho,e_k} \\ \mathcal{F}_{\rho\tilde{U},e_k} \\ \mathcal{F}_{\rho\tilde{V},e_k} \\ \mathcal{F}_{E,e_k} \end{pmatrix} = \int u \begin{pmatrix} 1 \\ u \\ v \\ \frac{1}{2}(u^2+v^2+\xi^2) \end{pmatrix} f(x_{j+1/2}, 0, t, u, v, \xi) \mathrm{d}\Xi,$$

where

$$\tilde{U} = U\cos\phi + V\sin\phi, \quad \tilde{V} = -U\sin\phi + V\cos\phi,$$

and ϕ is the angle between the normal direction and x-axis. So, the fluxes across the interface between the cell j and the cell $j+1$ (cf. Fig. 1) for the update of the conservative variables can be written as

$$\begin{pmatrix} \mathcal{F}_{\rho,e_k} \\ \mathcal{F}_{\rho U,e_k} \\ \mathcal{F}_{\rho V,e_k} \\ \mathcal{F}_{E,e_k} \end{pmatrix} = \begin{pmatrix} \mathcal{F}_{\rho,e_k} \\ \mathcal{F}_{\rho\tilde{U},e_k}\cos\phi - \mathcal{F}_{\rho\tilde{V},e_k}\sin\phi \\ \mathcal{F}_{\rho\tilde{U},e_k}\sin\phi + \mathcal{F}_{\rho\tilde{V},e_k}\cos\phi \\ \mathcal{F}_{E,e_k} \end{pmatrix}.$$

Therefore, the numerical flux $\mathcal{F}_{w,e_k}$ can be used to get w^{n+1}_j immediately by (3.4) (i.e. (3.5)).

What remains to finish is the description of our algorithm in the construction of the slopes $\mathrm{d}w^{n+1}_{j,j+1/2}$, $\mathrm{d}w^{n+1}_{j,j-1/2}$, $\mathrm{d}w^{n+1}_{j,j-3/2}$ of w_j at the cell interfaces at the $(n+1)$th time level. We should point out here that in the construction of our scheme, the most important is that one can extract more information (e.g. the value of the conservative variables at the points $\vec{x}_{j-3/2}, \vec{x}_{j-1/2}, \vec{x}_{j+1/2}$ on the cell boundary) from the time accurate gas distribution function f at the cell interface (see Fig. 1), from which we can therefore evaluate not only the fluxes but also the conservative flow variables there at the $(n+1)$th time level. This avoid using the values of the conservative variables from the neighboring cells in the construction of the slopes of w^{n+1}_j, and therefore, the scheme is computationally efficient. As is well-known, it is very difficult to choose a suitable stencil to construct slopes of w^{n+1}_j on an unstructured mesh, especially for high-order methods.

Hence for the cell j, at time step $n+1$, we have both the updated cell averaged value w_j^{n+1} and the three values $w_{j+1/2}^{n+1}, w_{j-1/2}^{n+1}, w_{j-3/2}^{n+1}$ at three interface points $\vec{x}_{j-3/2}, \vec{x}_{j-1/2}, \vec{x}_{j+1/2}$. Denote the value of the conservative variable at the cell interface between the cell j and the cell $j+1$ by

$$w_{j+1/2}^{n+1} = (\rho_{j+1/2}^{n+1}, \rho U_{j+1/2}^{n+1}, \rho V_{j+1/2}^{n+1}, E_{j+1/2}^{n+1}).$$

Then, we can obtain $w_{j+1/2}^{n+1}$ by integrating the time-dependent gas distribution function as follows:

$$w_{j+1/2}^{n+1} = \int \begin{pmatrix} 1 \\ u \\ v \\ \frac{1}{2}(u^2+v^2+\xi^2) \end{pmatrix} f(x_{j+1/2}, 0, t_{n+1}, u, v, \xi) \mathrm{d}\Xi.$$

Consequently, the slope of the conservative variables w^{n+1} at time step t_{n+1} inside the cell j along the normal direction of the cell interface between the cell j and the cell $j+1$ can be obtained by taking appropriate differences directly,

$$s_{j,j+1/2}^{+} = (w_{j+1/2}^{n+1} - w_j^{n+1})/\mathrm{d}n_+, \quad s_{j,j+1/2}^{-} = (w_j^{n+1} - \overline{w}^{n+1})/\mathrm{d}n_-,$$

where $\overline{w}^{n+1}$ is the average of $w_{j-1/2}$ and $w_{j-3/2}$, $\mathrm{d}n_+$ is the projection of $d_{j,j+1/2}$ in the normal direction, and $\mathrm{d}n_-$ is the projection of $d_{j,j-1/2}$ in the normal direction, $d_{j,j+1/2}$ is the distance from the centroid of the cell j to the interface point $j+1/2$, $d_{j,j-1/2}$ is the distance from the centroid of the cell j to the center between the interface points $j-1/2$ and $j-3/2$.

Having had the slopes $s_{j,j+1/2}^{\pm}$, thus we can use van Leer's limiter to obtain easily the slope $\mathrm{d}w_{j,j+1/2}^{n+1}$ of the conservative variables in the cell j along the normal direction of the cell interface between the cell j and the cell $j+1$, see Fig. 2. The slopes along the other two normal directions for the cell j can be obtained in the same manner. Hence, we have constructed $(w_j^{n+1}, \mathrm{d}w_{j,j+1/2}^{n+1}, \mathrm{d}w_{j,j-1/2}^{n+1}, \mathrm{d}w_{j,j-3/2}^{n+1})$ and finished the description of our algorithm.

3.2. An efficient continuous kinetic scheme for incompressible flows

For incompressible isothermal flows, the system (3.4) becomes in componentwise

$$\begin{cases} \rho^{n+1} = \rho^n - \int_{t_n}^{t_{n+1}} \sum\limits_{e_k \in \partial\Omega_j} \mathcal{F}_{\rho,e_k}(t)|e_k|/|\Omega_j|, \\ (\rho u)^{n+1} = (\rho u)^n - \int_{t_n}^{t_{n+1}} \sum\limits_{e_k \in \partial\Omega_j} \mathcal{F}_{\rho u,e_k}(t)|e_k|/|\Omega_j|, \\ (\rho v)^{n+1} = (\rho v)^n - \int_{t_n}^{t_{n+1}} \sum\limits_{e_k \in \partial\Omega_j} \mathcal{F}_{\rho v,e_k}(t)|e_k|/|\Omega_j|. \end{cases} \tag{3.7}$$

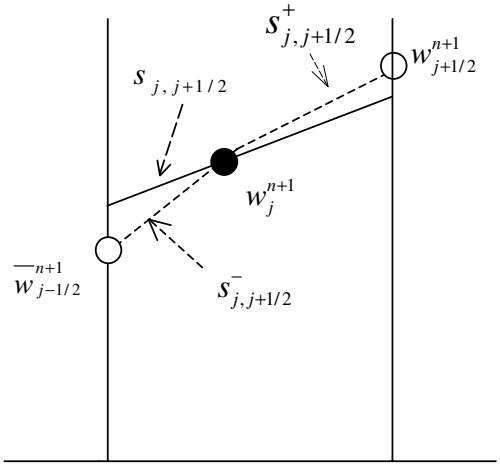

Fig. 2. Slope $s_{j,j+1/2}$ for the cell j along the normal direction of the interface between the cells j and $j+1$.

From Section 2, we see that this is just the finite volume scheme of the system (2.5). So, we only need to construct the flux $\mathcal{F}_{\rho,e_k}$ across an edge e_k. We will present a second-order continuous gas-kinetic BGK type scheme which is constructed using the time-dependent gas distribution function with continuous particle velocity in the evaluation of the numerical flux across cell interfaces.

Denote the location of the interface, such as the point $\vec{x}_{j+1/2}$ in Fig. 1, as $\vec{x}_0 = (0,0)$. The initial gas distribution f_0 around the point $\vec{x}_0$ at time $t = 0$ is assumed to have the form which is continuous in $\vec{x}$

$$f_0(\vec{x}) = g(\vec{x}_0, 0) + f^1(\vec{x}_0) + (\vec{x} - \vec{x}_0) \cdot \nabla g, \tag{3.8}$$

where the equilibrium state $g(\vec{x}_0, 0)$ has the same form as that in (2.4), and f^1 is a non-equilibrium state. For the isothermal Navier–Stokes equations, $\lambda = 1/(2\theta)$ is a constant. With a given Mach number M, λ is determined by

$$\lambda = M^2/(2u_\infty^2),$$

where u_∞ is the inflow velocity at infinity. Based on the Chapman–Enskog expansion [3], the non-equilibrium state becomes

$$f^1 = -\tau(g_t + ug_x + vg_y).$$

Recalling (2.4), and taking the temporal and spatial derivatives of the equilibrium distribution g, we have

$$\begin{cases} g_t = (A_1 + A_2 u + A_3 v)g, \\ g_x = (a_1 + a_2 u + a_3 v)g, \\ g_y = (b_1 + b_2 u + b_3 v)g, \end{cases} \tag{3.9}$$

where $\vec{x} = (x, y)$, and

$$A_1 = \frac{\rho_t}{\rho}\frac{\lambda}{\pi} - 2\lambda U U_t - 2\lambda W W_t, \quad A_2 = 2\lambda U_t, \quad A_3 = 2\lambda V_t,$$

$$a_1 = \frac{\rho_x}{\rho}\frac{\lambda}{\pi} - 2\lambda U U_x - 2\lambda W W_x, \quad a_2 = 2\lambda U_x, \quad a_3 = 2\lambda V_x,$$

$$b_1 = \frac{\rho_y}{\rho}\frac{\lambda}{\pi} - 2\lambda U U_y - 2\lambda W W_y, \quad b_2 = 2\lambda U_y, \quad b_3 = 2\lambda V_y.$$

The equilibrium distribution around the point $(\vec{x}_0, t_0)$ can be expanded into

$$\begin{aligned} g(\vec{x}, t) &= g(\vec{x}, t_0) + (x - x_0)\frac{\partial g}{\partial x} + (y - y_0)\frac{\partial g}{\partial y} + (t - t_0)\frac{\partial g}{\partial t} \\ &= g(\vec{x}, t_0)(1 + a(x - x_0) + b(y - y_0) + A(t - t_0)). \end{aligned} \tag{3.10}$$

Here the coefficients a_i can be found by taking the moments as follows:

$$\int \begin{pmatrix} 1 \\ u \\ v \end{pmatrix} (a_1 + a_2 u + a_3 v) g \, \mathrm{d}\Xi = \begin{pmatrix} \frac{\partial \rho}{\partial x} \\ \frac{\partial(\rho U)}{\partial x} \\ \frac{\partial(\rho V)}{\partial x} \end{pmatrix}, \tag{3.11}$$

where $(\frac{\partial \rho}{\partial x}, \frac{\partial(\rho U)}{\partial x}, \frac{\partial(\rho V)}{\partial x})$ is the projection in the x-direction of $(\frac{\partial \rho}{\partial n}, \frac{\partial(\rho U)}{\partial n}, \frac{\partial(\rho V)}{\partial n})$ which is the slope of the conservative variables in the cell j along the normal direction of a cell interface, and is given at the nth time level. The coefficients b_i are obtained in the same manner using the y-directional derivative of $(\rho, \rho U, \rho V)$ obtained by projecting $(\frac{\partial \rho}{\partial n}, \frac{\partial(\rho U)}{\partial n}, \frac{\partial(\rho V)}{\partial n})$ in the y-direction, while A_i are obtained from the compatibility condition:

$$\int\int \begin{pmatrix} 1 \\ u \\ v \end{pmatrix} f^1 \, \mathrm{d}u \, \mathrm{d}v = 0.$$

Now, all (unknown) terms in f_0 on the right-hand side of (3.8) and g on the right-hand side of (3.10) have been determined. Then, substituting f_0 and g into the integral solution (3.1), we get the gas distribution function around $(\vec{x}_0, 0)$ at the cell interface

$$f(x,y,t,u,v) = \frac{1}{\tau}\int_0^t (1 + a(x - u(t-t') - x_0) + b(y - v(t-t') - y_0) + At')g e^{-(t-t')/\tau}\,dt' + [1 + a(x - ut' - x_0) + b(y - vt' - y_0) - \tau(au + bv + A)]g e^{-t/\tau} = [1 - \tau(au + bv + A) + At]g.$$

Therefore, the numerical flux across the edge e_k is given by

$$\begin{pmatrix} \mathcal{F}_{\rho,e_k} \\ \mathcal{F}_{\rho\tilde{U},e_k} \\ \mathcal{F}_{\rho\tilde{V},e_k} \end{pmatrix} = \int u \begin{pmatrix} 1 \\ u \\ v \end{pmatrix} (1 - \tau(au + bv + A) + At)\rho_0 \left(\frac{\lambda}{\pi}\right) e^{-\lambda[(u-\tilde{U})^2 + (v-\tilde{V})^2]}\,d\Xi, \tag{3.12}$$

where

$$\tilde{U} = U\cos\phi + V\sin\phi, \quad \tilde{V} = -U\sin\phi + V\cos\phi,$$

and ϕ is the angle between the normal direction of the edge e_k and x-axis.

Integrating the flux (3.12) to the whole time step, we can obtain the total mass and momentum transport across the cell edges by (3.4). The flow variables inside each control volume are subsequently updated, and hence we have obtained w_j^{n+1}. Finally, the slopes $(\frac{\partial\rho}{\partial n}, \frac{\partial(\rho U)}{\partial n}, \frac{\partial(\rho V)}{\partial n})$ along the normal direction of cell interfaces at the $(n+1)$th time level are determined by interpolating directly the neighboring cell averaged values in the same manner as described at the end of Section 3.1. The above procedure can be repeated in the next time level. The description of our algorithm is complete.

4. Numerical examples

We now present six numerical examples, four for the compressible unsteady flow simulation, and two for the incompressible steady flow simulation, to validate the schemes. In all cases, the numerical time step is taken as

$$\Delta t = \mathrm{CFL}\min_j \sqrt{|\Omega_j|}/(\max|u| + c),$$

where CFL is the CFL number and c is the sound speed. In our numerical examples, CFL = 0.25–0.45 is used. The collision time τ is taken as

$$\tau = \epsilon\Delta t + \frac{|p_l - p_r|}{p_l + p_r}\Delta t \text{ for the compressible case, and } \tau = \frac{2\lambda}{\mathrm{Re}} \text{ for the incompressible case,}$$

where ϵ is a parameter.

The convergence test is made for two two-dimensional unsteady flow examples, for which the numerical results with different mesh sizes are presented.

Example 1. Sod's shock problem.

This problem has been extensively studied (see, e.g. [10,12,20]). It is a one-dimensional shock tube problem with two different initial constant states in the left and right part of the tube with unit length:

$$(\rho_l = 1, \rho_l U_l = 0, E_l = 2.5), \quad (\rho_r = 0.125, \rho_r U_r = 0, E_r = 0.5); \quad \text{and} \quad \gamma = 1.4,$$

and the initial discontinuity is located at $x = 1/2$. We present here the numerical results for the density distributions with 200 grid points and $\epsilon = 0.54$ using both the second-order scheme and the first-order scheme in Fig. 3. We see that they are generally in good agreement with the corresponding numerical results in [10,12,20], and the second-order scheme resolves shock and contact discontinuity wave better than that from the first-order scheme.

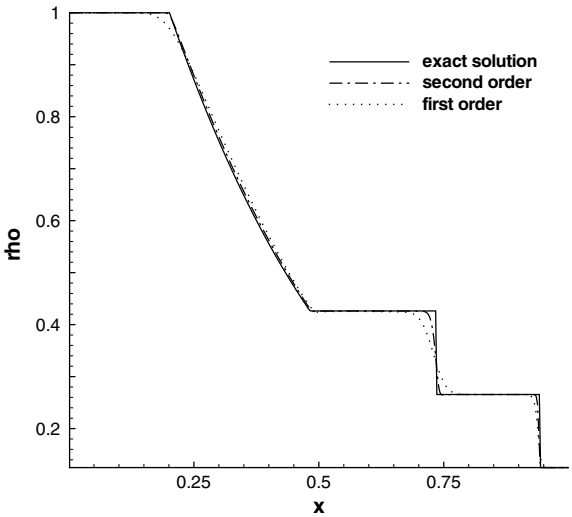

Fig. 3. Density distributions of the shock tube test from first and second-order schemes.

Example 2. A Mach 3 wind tunnel with a forward step.

This problem was extensively studied by Woodward and Colella [19], and later by many others. The setup of the problem is the following: A right going Mach 3 uniform flow enters a wind tunnel of one length unit wide and three length units long, where a step with 0.2 unit high is located at 0.6 unit from the left-hand end of the tunnel. Reflection boundary conditions are applied along the walls of the tunnel, and inflow and outflow conditions are applied at the entrance and exit, respectively. Here we give two density contours for different meshes with $\epsilon = 0.4$. The numerical result with 15,110 cells and 7759 nodes is shown in Fig. 4, while the numerical result with 59,466 cells and 30,137 nodes is presented in Fig. 5. The corner of the step is the center of a rarefaction fan and hence is a singular point of the flow. In our simulation, no special treatment was done at this singular point. It is easy to see that the numerical results here are comparable to those in [19]. In order to make the Mach stem above the low boundary shorter, special boundary treatment was done near the corner of the step in [19].

Example 3. Double Mach reflection of a strong shock.

This problem has also been extensively studied by Woodward and Colella [19], and by many others. We use exactly the same setup as in [19]. Namely, a Mach 10 shock initially makes a 60° angle with a reflecting wall. The undisturbed air ahead of the shock has a density of 1.4 and a pressure of 1. Here we give two density

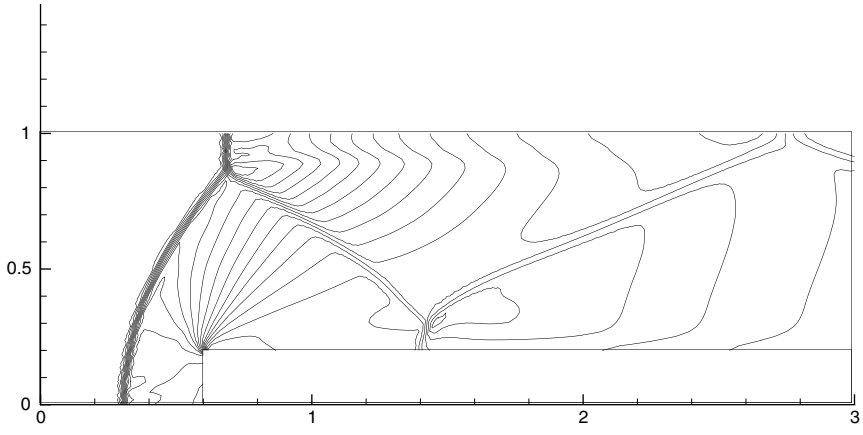

Fig. 4. Density contour of forward step problem on an unstructured mesh with 7759 nodes and 15,110 cells.

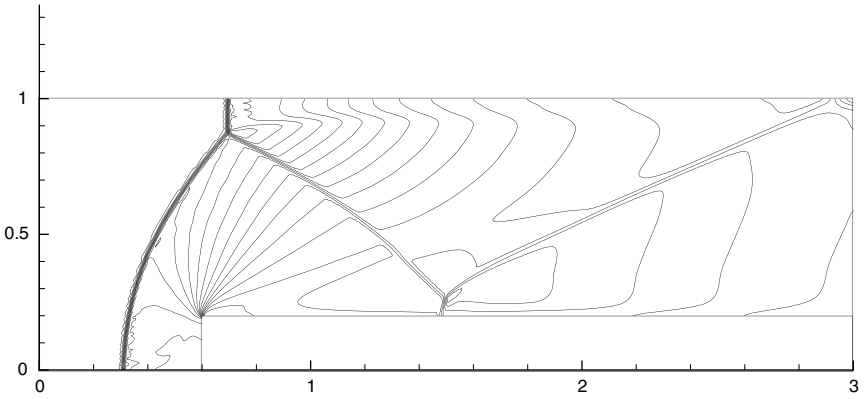

Fig. 5. Density contour of forward step problem with 30,137 nodes and 59,466 cells.

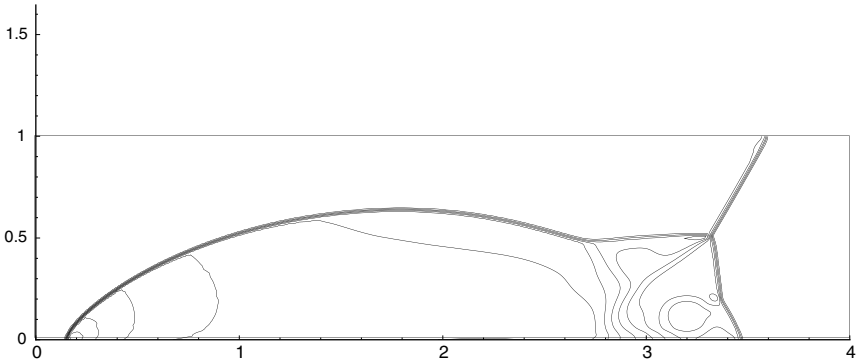

Fig. 6. Density contour of Mach reflection test on an unstructured mesh with 47,258 nodes and 93,510 cells.

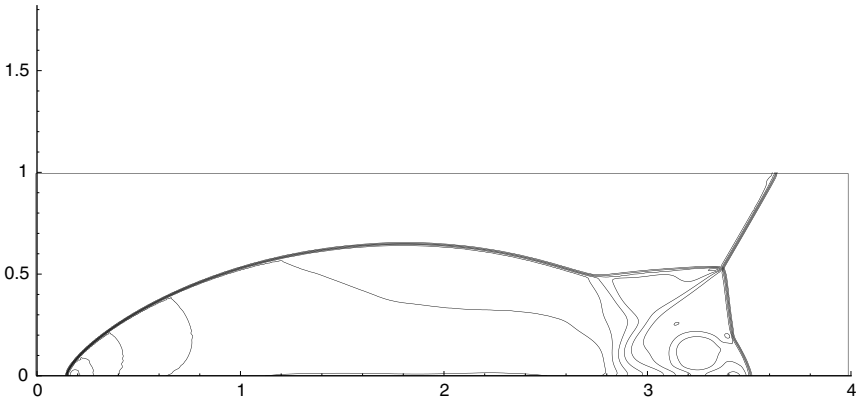

Fig. 7. Density contour of Mach reflection test with 96,137 nodes and 194,665 cells.

contours for different meshes with $\epsilon = 0.4$. The numerical result with 93,510 cells and 47,258 nodes is shown in Fig. 6, while the numerical result with 194,665 cells and 96,137 nodes is given in Fig. 7. Obviously, the numerical results here reproduce both in large scale and certain small scale those in [19], and those in the other literatures (e.g. [20]).

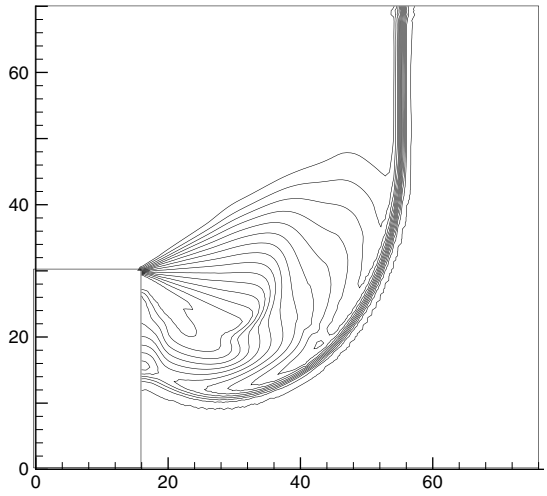

Fig. 8. Density contour of shock diffraction test with 9586 nodes and 18,792 cells.

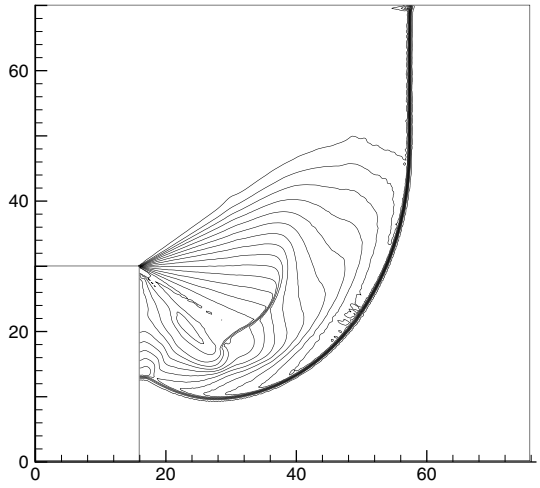

Fig. 9. Density contour of shock diffraction test on a refined mesh with 83,406 nodes and 165,684 cells.

Example 4. Diffraction around a corner.

This problem was studied by Quirk in [18]. It is a strong shock of Mach number 5.09 diffraction around a corner. It is well known that the original Godunov scheme, the Roe scheme without any entropy-fix and the Osher scheme could yield a "shock" at the rarefaction corner (see [18]). Here, we show the numerical results of two density contours with different meshes and $\epsilon = 0.4$. The results with 18,792 cells and 9586 nodes are given in Fig. 8, while the result with 165,684 cells and 83,406 nodes in Fig. 9. There are no detections or entropy-fix in our calculation. From Figs. 8 and 9 we see that the simulated results here reproduce the large-scale structure of the corresponding numerical and experiment results in [1,9]. From Examples 2–4 we find that as the mesh is refined, the numerical solutions are getting convergent.

Example 5. Cavity flow.

The laminar incompressible flow inside a square cavity with a moving top boundary is a well-defined test for the code verification in spite of the singularities at four corners. For variable Reynolds numbers, highly accurate solutions have been obtained by Ghia [7], where a finite difference scheme with stream vorticity formulation was used for the solutions. In this test, the computational domain is $[0,1]\times[0,1]$, the upper boundary is moving with a velocity $u_0 = 1.0$, and the isothermal temperature takes a value to have an

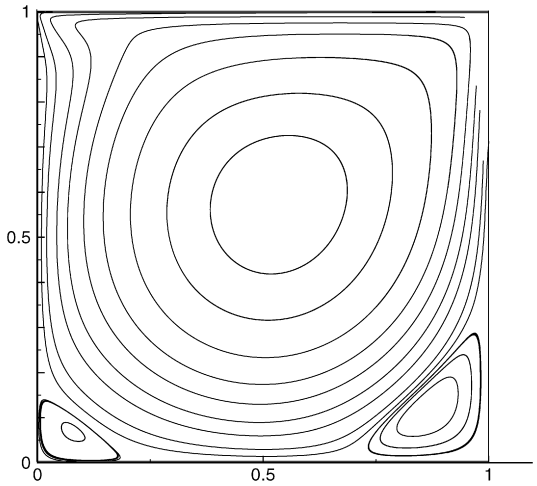

Fig. 10. Stream lines inside a cavity at $Re = 1000$ on an unstructured mesh with 12,106 nodes and 23,800 cells.

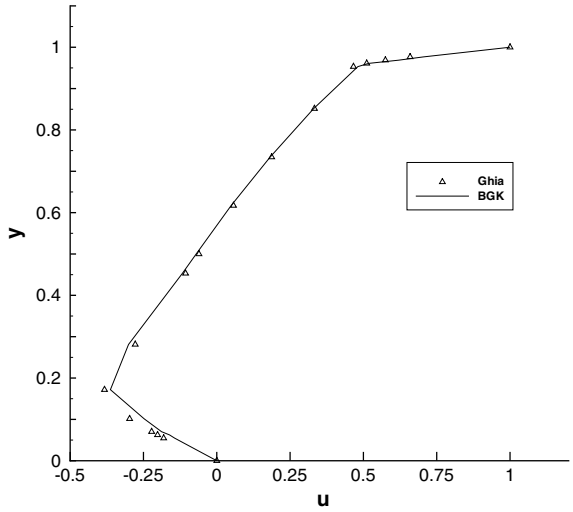

Fig. 11. U velocity distribution along a center vertical line, where the solid line is the result from the current scheme and the triangles are the benchmark solution from [7].

equivalent Mach number 0.15 for the flow inside the cavity. Non-slip boundary conditions are used for the other three cavity boundaries. The viscosity coefficient is determined by $v = u_0 L/Re$, where $L = 1$ and the Reynolds number has a value 1000. The computation with 12,106 nodes and 23,800 mesh cells is carried out, and totally, 200,000 time steps are used in order to get a steady state solution. The computed stream line and velocity are shown in Figs. 10–12, from which we find that our numerical results reproduce accurately Ghia's benchmark solution.

Example 6. Back step flow.

Laminar flow over a back-facing step in a two-dimensional channel is also a well-defined benchmark test case. The associated flow separation and subsequent reattachment in this case have been recognized as important phenomena in engineering problems. For example, the flow separation is undesirable in many cases, which leads to the unwanted pressure drops and energy losses. The setup of back-step domain is 45 mm width, 250 mm length, and a channel with 15 mm width, where an unstructured mesh with 12,697 cells and 6565 nodes is generated. Non-slip boundary conditions on the upper and lower boundaries are used, where the

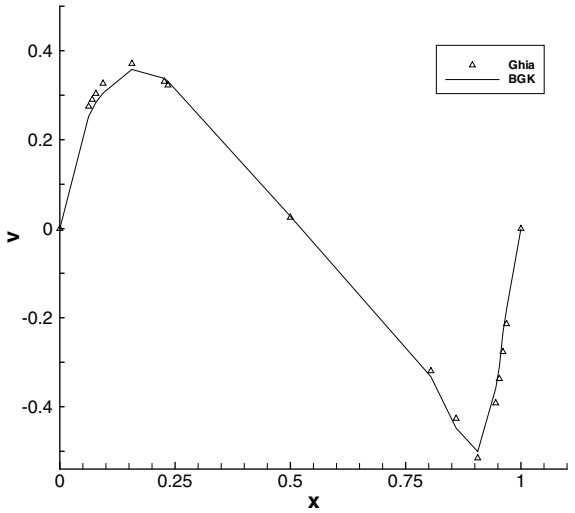

Fig. 12. V velocity distribution along a center horizontal line, where the solid line is the result from the current scheme and the triangles are the benchmark solution from [7].

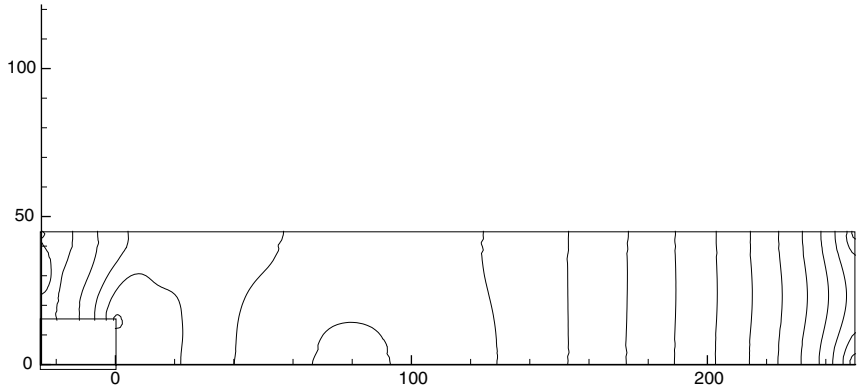

Fig. 13. Pressure distribution inside a back-facing step channel at $Re = 73$.

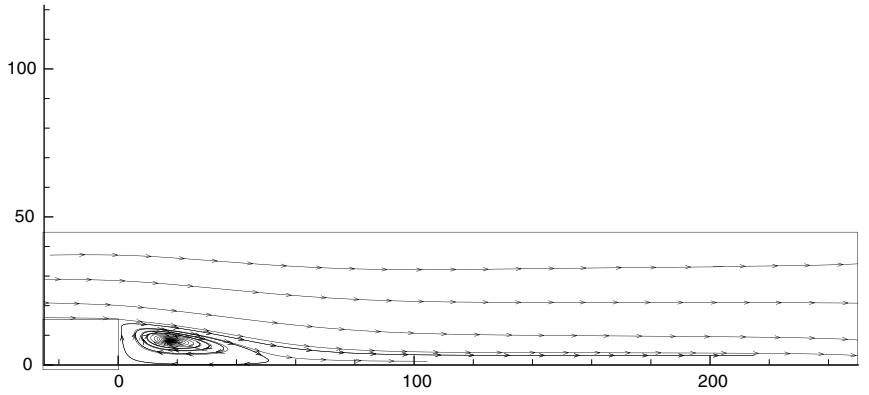

Fig. 14. Stream lines distributions inside the channel.

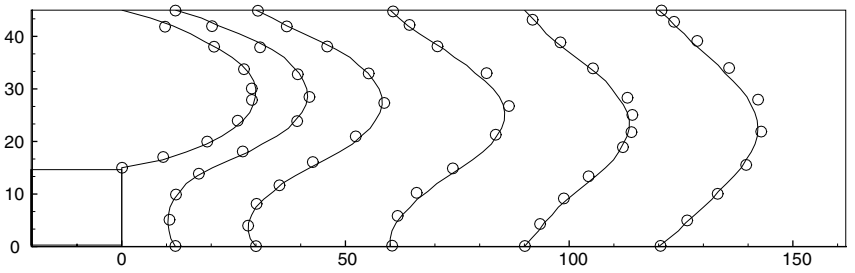

Fig. 15. U velocity distributions at different locations of $x = 0.0$, 12.0, 30.0, 60.0, 90.0, and 120.0, where the circles are the experimental results from [5].

inflow and outflow conditions for the left and right entrances are imposed. A parabolic inflow fluid velocity is implemented on the left boundary with a maximum velocity 0.72, and Reynolds number 73 is imposed in the current simulation. The experimental measurements as well as our numerical results are shown in Figs. 13–15, where the pressure, stream lines, and the flow velocities at different cross sections are presented. Obviously, the numerical results here are in good agreement with the experiment by Denham [5].

5. Conclusion

In this paper, we present efficient kinetic schemes on unstructured meshes for compressible unsteady and incompressible steady flow computations, respectively. For compressible flow, we use the time-dependent gas distribution function to get both the fluxes and the flow variables at cell interfaces to construct a second-order gas-kinetic BGK scheme. For an incompressible flow, the gas-kinetic BGK scheme is extended to the simulation of isothermal incompressible flows on unstructured meshes, on which a continuous gas distribution function is used. The efficiency of the schemes is due to the implementation that the slopes of flow variables inside each cell can be constructed using only the values inside that cell as well as those on the cell interface. Subsequently, the method avoids using the values from neighboring cells. All these are solely rooted in the special property of the gas-kinetic BGK formulation, where a time accurate gas distribution function at a cell interface is constructed. Therefore, even with the stencil of a first-order scheme, a high resolution scheme can be obtained. Even though only a second-order accuracy method is presented in this paper, the methodology in this paper can be naturally extended to even higher-order scheme, because for higher-order method the gas distribution functions at more interface points can be evaluated and be used to obtain high-order reconstruction inside each cell. Numerical examples for steady and unsteady flows are presented in this paper, which demonstrate the efficiency and accuracy of the schemes.

Acknowledgments

This work was supported by the Special Funds for Major State Basic Research Projects, the NSFC (Grant No. 10225105), and by the fund of Chinese academy of engineering physics (No.20060644). K. Xu was supported by Hong Kong Research Grant Council through RGC HKUST621005, 621406.

References

[1] S.K. Bazhenova, L.G. Gvozdeva, M.G. Nettleton, Unsteady interactions of shock waves, Prog. Aerospace Sci. 21 (1984) 249–331.
[2] P.L. Bhatnagar, E.P. Gross, M. Krook, A model for collision processes in gases I: Small amplitude processes in charged and neutral one component systems, Phys. Rev. 94 (1954) 511–525.
[3] S. Chapman, T.G. Cowling, The Mathematical Theory of Non-Uniform Gases, Cambridge Univ. Press, 1990.
[4] S.Y. Chen, G.D. Doolen, Lattice Boltzmann method for fluid flows, Ann. Rev. Fluid Mech. 30 (1998) 329–367.
[5] M.K. Denham, M.A. Partrick, Laminar flow over a downstream facing step in a two dimensional flow channel, Trans. Inst. Chem. Eng. 52 (1997) 361–367.
[6] S.M. Deshpande, A second order accurate, kinetic-theory based, method for inviscid compressible flows. NASA Langley Tech. Paper No. 2613, 1986.

[7] U. Ghia, K.N. Ghia, C.T. Shin, High resolutions for imcompressible flow using the Navier–Stokes equations and a multigrid method, J. Comput. Phys. 48 (1982) 387–411.
[8] X.Y. He, L.S. Luo, Theory of the lattice Boltzmann method: From the Boltzmann equation to the lattice Boltzmann equation, Phys. Rev. E 56 (6) (1997) 6811–6817.
[9] R. Hillier, Computation of shock wave diffraction at a ninety degrees convex edge, Shock Waves 1 (1991) 89–98.
[10] S. Karni, Multicomponent flow calculations by a consistent primitive algorithm, J. Comput. Phys. 112 (1994) 31–43.
[11] C. Kim, A. Jameson, A robust and accurate LED-BGK solver on unstructured adaptive meshes, J. Comput. Phys. 143 (1998) 598–627.
[12] B. Larrouturou, How to preserve the mass fraction positive when computing compressible multi-component flow, J. Comput. Phys. 95 (1991) 59–84.
[13] G. May, A. Jameson, Unstructured algorithm for the inviscid and viscous flows embedded in a unified solver architecture: Flo3xx, Paper 2005-0318, 2005.
[14] G. May, B. Srinivasan, A. Jameson, An improved gas kinetic BGK finite volume method for three dimensional transonic flow, J. Comput. Phys. 220 (2007) 856–878.
[15] T. Ohwada, On the construction of kinetic scheme, J. Comput. Phys. 177 (2002) 156–175.
[16] T. Ohwada, K. Xu, The kinetic scheme for the full Burnett equations, J. Comput. Phys. 201 (2004) 315–332.
[17] D.I. Pullin, Direct simulation methods for compressible inviscid ideal gas flow, J. Comput. Phys. 34 (1980) 231–244.
[18] J. Quirk, A contribution to the great Riemann solver debate, Int. J. Numer. Meth. Fluids 18 (1994) 555–574.
[19] P. Woodward, P. Colella, The numerical simulation of two dimensional fluids with strong shock, J. Comput. Phys. 54 (1984) 115–173.
[20] K. Xu, Gas kinetic scheme for unsteady compressible flow simulations, Von Kárman Institute for Fluid Dynamics, Lecture Note Series 1998-03 (1998).
[21] K. Xu, A gas-kinetic BGK scheme for the Navier–Stokes equations and its connection with artificial dissipation and Godunov method, J. Comput. Phys. 171 (2001) 289–335.
[22] K. Xu, A slope update scheme for compressible flow simulation, J. Comput. Phys. 178 (2002) 252–259.